Volume 147
Number 9
7 May 2022
Pages 1745-2010

Analyst

rsc.li/analyst

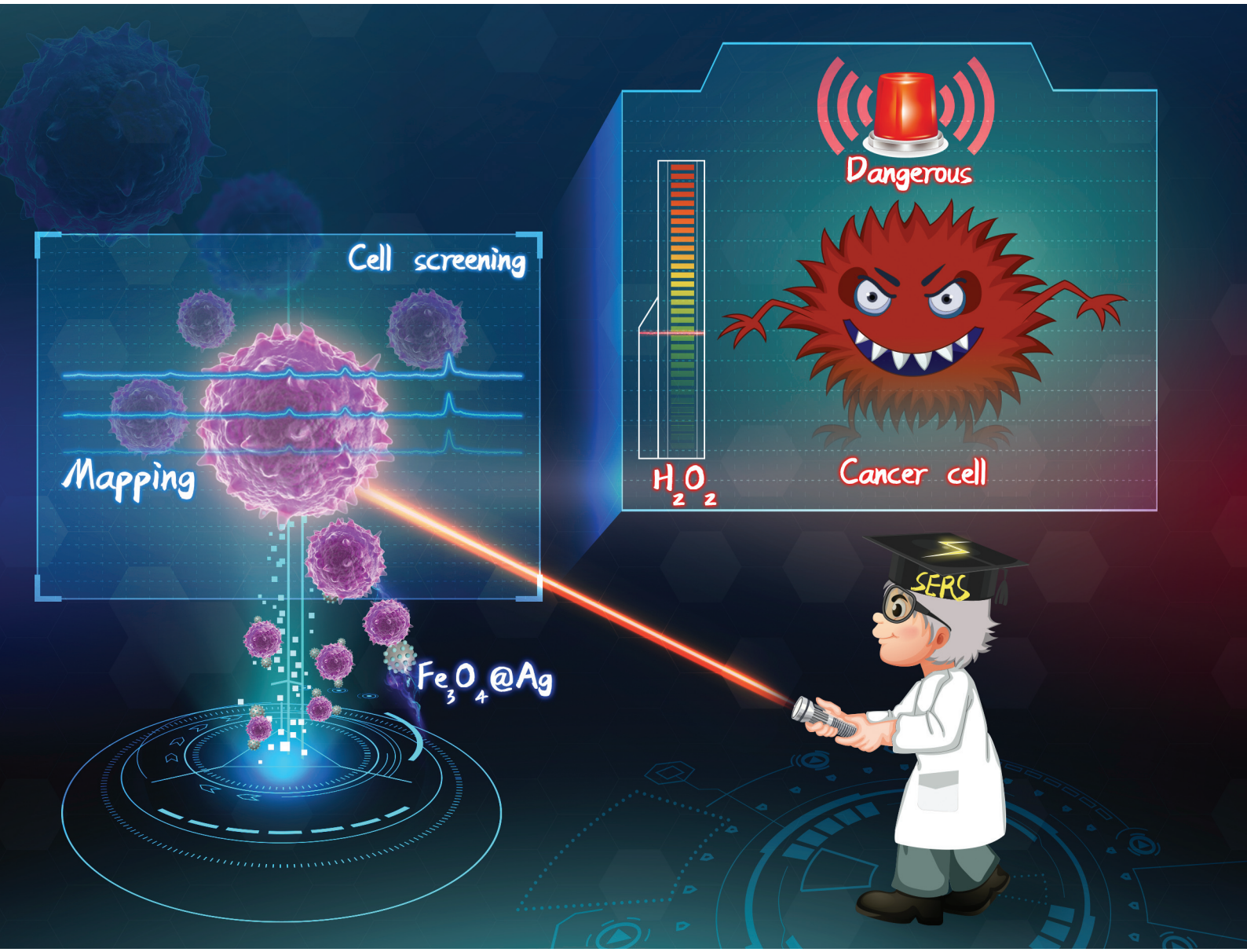

ISSN 0003-2654

ROYAL SOCIETY OF CHEMISTRY

PAPER

Yue Wang, Zhangrun Xu, Yukihiro Ozaki *et al.*
In situ SERS monitoring of intracellular H_2O_2 in single living cells based on label-free bifunctional Fe_3O_4@Ag nanoparticles

Analyst

PAPER

View Article Online
View Journal | View Issue

Check for updates

Cite this: *Analyst*, 2022, **147**, 1815

Published on 17 Februarie 2022. Downloaded on 2025-08-07 10:22:05 vm..

In situ SERS monitoring of intracellular H_2O_2 in single living cells based on label-free bifunctional Fe_3O_4@Ag nanoparticles†

Yue Wang, *[a] Cheng Cheng,[a] Ruofei Ma,[a] Zhangrun Xu *[a] and Yukihiro Ozaki *[b]

Visualization of signaling molecules in single living cells is crucial for understanding cellular metabolism and physiology, which can provide valuable insights into early diagnoses and treatments of diseases. Highly sensitive *in situ* monitoring of intracellular analytes released from single living cells by virtue of label-free nanosensors is urgently needed, which can avoid interferences from molecular labeling. Here, we proposed an ultrasensitive strategy for *in situ* imaging of intracellular H_2O_2 in single living cancer cells by surface-enhanced Raman scattering (SERS) spectroscopy with the utilization of label-free Fe_3O_4@Ag core–satellite nanoparticles (NPs). The Fe_3O_4@Ag NPs can efficiently and selectively catalyze the oxidation of the peroxidase substrate 3,3′,5,5′-tetramethylbenzidine (TMB) in the presence of H_2O_2. Additionally, they exhibit excellent SERS activity that allows for *in situ* monitoring of intracellular H_2O_2 in living cells through establishing the correlation between the H_2O_2 level and the SERS intensity of the catalytic oxidation product of TMB. The H_2O_2 concentration is revealed through the SERS intensity of oxidized TMB with a good linear response in a wide range from 1 fM to 1 mM. Moreover, the intracellular H_2O_2 level in live cancer cells and imaging of the distribution of H_2O_2 inside single cells can be achieved by using such a label-free nanosensor based strategy. Our work demonstrates that the label-free Fe_3O_4@Ag NP-based SERS imaging and quantification strategy is a promising and powerful approach to assess intracellular H_2O_2 in living cells and allows us to monitor single-cell signaling molecules with nanoscale resolution.

Received 7th January 2022,
Accepted 17th February 2022

DOI: 10.1039/d2an00035k

rsc.li/analyst

1. Introduction

Hydrogen peroxide (H_2O_2) is one of the representatives of reactive oxygen species (ROS) generated from aerobic metabolism in cells,[1] and has been verified to be an essential signaling molecule that is closely associated with signal transduction pathways involved in diverse cellular processes.[2,3] H_2O_2 plays a vital role in maintaining cellular homeostasis, and it influences the biological functions in a concentration-dependent manner.[4] A normal level of H_2O_2 is crucial for physiological processes of cells. However, excess H_2O_2 will cause intracellular oxidative stress, leading to malignant transformation of cells and various diseases, and even cancers.[5] An endogenous H_2O_2 level can also be regarded as a biological indicator to reflect the development and progression of cancer cells.[6] Considering the significance of H_2O_2 in cellular physiology and pathology, the *in situ* ultrasensitive and reliable visualization measurement of intracellular H_2O_2 in living cells is essential for the early diagnosis and effective therapy of various diseases.[7] However, bulk cell measurement usually gives population-averaged results that cover cellular heterogeneity and hinder the investigation and identification of very few abnormal cells which are highly related to disease progression and exacerbation.[8] Therefore, *in situ* visualized monitoring of intracellular H_2O_2 in single living cells is crucial for better understanding the cellular behavior and heterogeneity of tumor cells, which can provide a valuable insight into improving cancer screening rates and reducing cancer-related mortality. However, *in situ* visualization and quantification of intracellular H_2O_2 in single cells are challenging due to the micrometer scale of cells, the ultralow con-

[a]*Department of Chemistry, College of Sciences, Northeastern University, Shenyang 110819, PR China. E-mail: yuewang@mail.neu.edu.cn, xuzr@mail.neu.edu.cn*
[b]*School of Biological and Environmental Sciences, Kwansei Gakuin University, Sanda, Hyogo 669-1337, Japan. E-mail: ozaki@kwansei.ac.jp*

†Electronic supplementary information (ESI) available: XRD and magnetization curve characterization, optimization of reaction conditions of the Fe_3O_4@Ag NP catalytic reaction, verification of the production of $^{\bullet}OH$ by fluorescence and Raman spectra, stability of catalytic activity, Michaelis–Menten constants, maximum reaction rates, and MTT-based cytotoxicity assay of Fe_3O_4@Ag NPs. See DOI: 10.1039/d2an00035k

Published on 17 Februarie 2022. Downloaded on 2025-08-07 10:22:05 vm..

centration of H_2O_2 in a single cell, and the interference of the intra/extracellular microenvironment.

With the development of various technologies, plenty of single-cell imaging techniques have emerged,[9–13] such as microscopy-based methods,[9] electrochemiluminescence imaging,[10] fluorescence imaging,[11] and optical diffraction tomography.[12] Although these approaches have made great progress in visualization analysis of single cells, they are usually time-consuming in sophisticated sample-preparation processes, complicated in operation that requires some seriously particular technical expertise, lacking sufficient sensitivity with label-free methods, or are greatly dependent on labeled probes with auto-fluorescence and photo-bleaching issues that may affect the results.[6,9–12,14,15] Consequently, an ultra-sensitive, effective, and feasible imaging method for *in situ* monitoring of intracellular H_2O_2 in single cells has been highly desired.

Surface-enhanced Raman scattering (SERS) spectroscopy is a nondestructive ultrasensitive analytical technique that has been considered as one of the most promising analytical tools and extensively applied for imaging of biologically relevant molecules in live cells.[16,17] SERS offers the advantages of ultrahigh sensitivity, high spectral specificity for multiplex detection, and superior resistance to auto-fluorescence and photobleaching.[17,18] To date, many labeled nanosensor-based SERS strategies have been exploited for the detection and imaging of H_2O_2 at the single-cell level, in which labeled reporter molecules with a strong Raman signal and sensitive chemical response to analytes are inevitable.[17–19] However, the labeled SERS imaging of intracellular H_2O_2 in living cells still has some problems that restrict its applications, such as the lack of the user-friendly SERS reporters for selective detection of H_2O_2 and poor signal reproducibility caused by the desorption/degradation of the reporter molecules in a physiological environment. Therefore, the development of a label-free nanosensor-based SERS approach for *in situ* monitoring of intracellular H_2O_2 in single living cells with ultrahigh sensitivity and reliability is in urgent demand.

The analytical performance of SERS-based measurement techniques largely depends on the advantage of nanomaterials, since the dramatic SERS enhancement is mainly derived from the strong localized surface plasmon resonance (LSPR) generated by plasmonic nanomaterials.[20–22] As an excellent SERS active substrate for bioassay applications, the nanomaterials need to not only produce a sufficiently strong plasmonic field and create abundant hot spots for improving SERS capability, but also possess high biocompatibility and sensitive response to the biomolecules to be detected.[17] Hybrid nanostructures, which integrate the advantages of the respective components and exhibit even superior properties to each component, have aroused extensive interest for various applications.[23–25] In this respect, a hybrid nanostructure with high SERS activity and a fast response function to H_2O_2 simultaneously can be beneficial for the visualization of cell morphology and the distribution of intra/extracellular H_2O_2. The hybrid NPs composed of Fe_3O_4 and Ag nanoparticles (NPs) retain the prominent SERS activity and the promising peroxidase-like catalytic activity. Numerous Fe_3O_4/Ag nanocompounds with diverse structures and morphologies have been developed for achieving superior performances in bioanalysis applications.[26,27] Among them, Fe_3O_4@Ag core–satellite nanostructures, possessing high SERS activity, good magnetic responsiveness, and great peroxidase-like catalytic activity, have attracted a great deal of attention.[27,28] Such nanostructures can generate strong plasmonic coupling between the Ag NPs, which significantly enhance electromagnetic fields by providing abundant hot spots for ultra-sensitive SERS measurement. Moreover, Fe_3O_4@Ag core–satellite NPs retain the inherent peroxidase-like catalytic activity of Fe_3O_4 NPs,[29] which can catalyze H_2O_2 to produce $^{\bullet}OH$, allowing for intracellular H_2O_2 detection in the presence of peroxidase substrates.

Herein, we presented an ultrasensitive strategy for *in situ* imaging and quantification of intracellular H_2O_2 in single living cancer cells by SERS spectroscopy using label-free Fe_3O_4@Ag core–satellite NPs, which displayed not only prominent SERS sensitivity but also excellent peroxidase catalytic activity and stability. In our case, the Fe_3O_4@Ag core–satellite NPs can efficiently and selectively catalyze H_2O_2 to produce $^{\bullet}OH$, which leads to further oxidation of the peroxidase substrate 3,3′,5,5′-tetramethylbenzidine (TMB). The H_2O_2 detection can thus be achieved through establishing the correlation between the concentration of H_2O_2 and the SERS intensity of the catalytic oxidation product of TMB. The label-free Fe_3O_4@Ag NP-based SERS strategy we proposed was successfully employed for *in situ* imaging and quantification of intercellular H_2O_2 in single living B16 (mouse melanoma) cells. This is a promising and powerful approach for the determination of intracellular H_2O_2 in single living cells, which can avoid the interference from molecular probes in comparison with labeled nanosensor-based methods. Our work shows great potential for investigating the roles of H_2O_2 in physiological and pathological processes of cells, which is conducive to the early diagnosis and effective follow-up therapy of H_2O_2-related diseases.

2. Experimental

2.1. Materials and chemicals

$HAuCl_4{\cdot}4H_2O$, ferric chloride ($FeCl_3{\cdot}6H_2O$), ethylene glycol (EG), sodium borohydride ($NaBH_4$), sodium acetate anhydrous (NaAc), polyvinylpyrrolidone (PVP, MW 40 000), silver nitrate ($AgNO_3$), acetic acid (CH_3COOH), formaldehyde (37%), ammonia (28%), and hydrogen peroxide (H_2O_2) were purchased from Sinopharm Chemical Reagent Co., Ltd. Polyethyleneimine branched (PEI, MW 10 000), phorbol myristate acetate (PMA), 3,3′,5,5′-tetramethyibenzidine (TMB), polyethylene glycol (PEG, MW 6000), 2,2′-azobis(2-methylpropionamidine)dihydrochloride (AAPH), trisodium citrate, inorganic salts, and other reagents were obtained from Aladdin Industrial Corporation (Shanghai, China). Terephthalic acid

 This journal is © The Royal Society of Chemistry 2022

Published on 17 Februarie 2022. Downloaded on 2025-08-07 10:22:05 vm..

(TA) and L-cysteine (L-Cys) were obtained from Sigma-Aldrich (Shanghai, China). B16F10 (B16) cells and 3-(4,5-dimethylthiazol-2-yl)-2,5-diphenyltetrazolium bromide (MTT) were purchased from Jiangsu Keygen Biotech Co., Ltd. The Roswell Park Memorial Institute (RPMI) 1640 medium was acquired from Biological Industries (Israel Beit Haemek, LTD). Fetal bovine serum (FBS) was purchased from Hyclone Thermo Fisher Scientific Inc. Trypsin, horseradish peroxidase (HRP) and glutathione (GSH) were obtained from Sangon Bioengineering Co., Ltd. Distilled and deionized water from a Milli-Q plus system with a resistivity greater than 18 MΩ cm was used throughout the experiment.

2.2. Instruments and measurement

The morphologies of the as-prepared nanoparticles were characterized employing transmission electron microscopy (TEM, Carl Zeiss, Jena, Thuringia, Germany) and scanning electron microscopy (SEM, Hitachi SU8010, Japanese). The X-ray diffraction (XRD) measurement was carried out on a Panalytical X'Pert Pro (PW 3040/60) (Panalytical B.V., Almelo, The Netherlands) with Cu Kα radiation to investigate the crystallographic structure of the products. The UV-vis absorption spectra of the solutions were obtained by using a microplate spectrophotometer (BioTek, Synergy H1) with a step size of 1 nm. The magnetic hysteresis loops were measured on a vibrating sample magnetometer operated (VSM-7300, LakeShore, USA) at room temperature. The excitation and emission spectra of the phosphors were measured with a Hitachi F-4500 fluorescence spectrophotometer.

SERS spectra were collected using a Raman microscope (XploRA ONE, Horiba Jobin Yvon France) with a laser wavelength of 638 nm. The cell imaging measurement was performed with an inVia Qontor confocal Raman microscope (Renishaw) with a laser excitation wavelength of 633 nm. The laser was focused on the surface of the sample using a 50× long-distance objective lens with 1 μm spot size, and the power of the laser was about 0.6 mW. All SERS spectra were obtained under the same conditions using a holographic grating of 1200 grooves per mm.

2.3. Synthesis of Fe_3O_4@Ag core–satellite NPs

Fe_3O_4 magnetic NPs were synthesized *via* a solvothermal method.[30] First, 1.35 g of $FeCl_3{\cdot}6H_2O$ was dissolved in 40 mL of EG under magnetic stirring for 30 min. Next, 2.7 g of NaAc and 1 g of PEG were added into the above solution with stirring for 2 h. The mixture was then transferred into a Teflon-lined stainless-steel autoclave (50 mL capacity) and heated at 210 °C for 6 h. After the autoclave was cooled down to room temperature, the magnetic Fe_3O_4 NPs were washed with deionized water and ethanol three times, respectively, and then dried in a vacuum at 60 °C for 6 h. Subsequently, the as-synthesized Fe_3O_4 NPs were surface-modified with a uniform PEI layer under sonication conditions.[31] In a typical procedure, 0.05 g of Fe_3O_4 NPs were dispersed in 30 mL of PEI solution (0.06 g mL^{-1}) under sonication for 2 h. The surface-modified Fe_3O_4 NPs were then magnetically separated and washed five times with deionized water. Next, the surface-modified Fe_3O_4 NPs were mixed with the Au seeds, which were prepared by the sodium borohydride reduction method,[32] to synthesize Fe_3O_4@Au NPs through electrostatic interaction. After rinsing, the Fe_3O_4@Au NPs were dispersed in 100 mL of deionized water. 20 mL of the purified Fe_3O_4@Au NP dispersion was added to 100 mL of silver nitrate (0.25 mM) aqueous solution containing 0.2 wt% PVP under ultrasonication. An excess amount of 37% formaldehyde (150 μL) and 25% ammonia solution (300 μL) were added in sequence with another 2 min of ultrasonication. Finally, the Fe_3O_4@Ag core–satellite NPs were obtained after thorough rinsing.

2.4. Peroxidase-like activity measurements of Fe_3O_4@Ag core–satellite NPs

The peroxidase-like activity of the Fe_3O_4@Ag core–satellite NPs was studied by investigating the oxidation of the peroxidase substrate TMB by H_2O_2 in acetate buffer (pH = 4.0, 10 mM) in the presence of Fe_3O_4@Ag. The reaction solution was incubated at room temperature for 30 min in the dark. The resulting reaction solution was measured by UV-vis spectroscopy and the time-dependent absorbance variation of the solution at 652 nm was monitored. The kinetic analyses of the Fe_3O_4@Ag core–satellite NP-catalysed reaction were performed subsequently.

2.5. Detection of hydroxyl radicals (·OH)

Generation of ·OH during the catalytic reaction process was monitored by photoluminescence (PL) spectroscopy with TA as the fluorescent probe, in which TA can react with ·OH to form strongly fluorescent 2-hydroxyterephthalic acid.[33] The fluorescence measurement was carried out with an excitation wavelength of 315 nm by using a freshly mixed solution prepared in sodium acetate buffer (pH 4.0), containing the same volume (20 μL) of 1 mM TA, 1 mg mL^{-1} Fe_3O_4@Ag NPs, and 2.5 mM H_2O_2.

2.6. SERS monitoring of catalytic oxidation of TMB by Fe_3O_4@Ag core–satellite NPs and SERS detection of H_2O_2

First, 20 μL of peroxidase substrate TMB (1.5 mM) and 20 μL of the prepared Fe_3O_4@Ag NP dispersion (1 mg mL^{-1}) were mixed together in the acetate buffer solution (10 mM, pH 4.0). Then, 20 μL of H_2O_2 (2.5 μM) aqueous solution was added into the above mixed solution to monitor the catalytic oxidation of TMB. For the detection of H_2O_2, the mixed solutions of TMB, H_2O_2, and Fe_3O_4@Ag NP dispersion were prepared with H_2O_2 concentrations in the range of 10^{-3} to 10^{-15} M.

2.7. Determination of cellular H_2O_2 by SERS

B16 (mouse melanoma) cells were cultured in RPMI 1640 supplemented with 10% FBS and 1% penicillin/streptomycin solution under the conditions of 5% CO_2 and 95% air atmospheres at 37 °C. When the B16 cells reached 80–90% confluence, they were separated from the culture flasks by treating with trypsin and grown at 37 °C for 24 h. After washing several times with PBS buffer (10 mM, pH = 7.4), the cells were dispersed in 2 mL

Published on 17 Februarie 2022. Downloaded on 2025-08-07 10:22:05 vm..

of PBS buffer. Then, 20 μL of PMA at a concentration of 5.0 μg mL^{-1} was added to the above cell suspension and incubated for 1 h to stimulate the cells to generate H_2O_2. Next, 20 μL of HRP (100 U mL^{-1}) was added to the diluted above solution to decompose H_2O_2. Next, 20 μL of the TMB solution (1.5 mM) and 20 μL of the Fe_3O_4@Ag NP dispersion (1 mg mL^{-1}) were added into the cell suspension with and without PMA treatment separately before the SERS measurement.

2.8. *In situ* SERS imaging of B16 cells

B16 cells were seeded in a 30 mm dish and cultured overnight until they adhered to the bottom of the dish. The B16 cells were further incubated with 20 μL of the Fe_3O_4@Ag NP (~2 μg mL^{-1}) dispersion at 37 °C for 24 h. Afterwards, the excess Fe_3O_4@Ag NPs present in the culture medium were removed by washing the cells three times with PBS. Then, the cells were incubated with PMA in culture medium at 37 °C for another 1 h. Finally, 20 μL of TMB solution (1.5 mM) was added into the above culture medium before SERS imaging. The SERS images were obtained within less than 15 min with 50× objective lens, a scanning step of 200 nm, and an exposure time of 0.01 s at 633 nm excitation.

2.9. Selectivity of Fe_3O_4@Ag core–satellite NPs

To examine the selectivity of the Fe_3O_4@Ag NPs toward H_2O_2, the SERS response was acquired using other anions, cations, thiols and other oxidative species. The testing solutions (1 mM) of NaCl, $NaCO_3$, $NaNO_2$, $NaNO_3$, $NaSO_4$, KCl, $CaCl_2$, $FeCl_2{\cdot}4H_2O$, $FeCl_3{\cdot}6H_2O$, L-Cys, and GSH were prepared with distilled water. Organic peroxide radicals ($ROO^{\bullet}$) were generated by pyrolyzing the AAPH (10 μM) solution at 37 °C. Peroxynitrite ($ONOO^-$) was acquired by the reaction of $NaNO_2$ (50 μM) with H_2O_2 (50 μM) in acidic solution. Singlet oxygen ($^1O_2$) was produced by the reaction of the NaClO (50 μM) solution with the H_2O_2 (50 μM) solution. The above-mentioned competitive ions, thiols and oxidative species were mixed with 20 μL of Fe_3O_4@Ag NPs (1 mg mL^{-1}) and 20 μL of TMB solution (1.5 mM) in 140 μL of PBS buffer (10 mM, pH 7.4) at 37 °C.

3. Results and discussion

3.1. Characterization of the Fe_3O_4@Ag NPs

The morphologies of the synthesized Fe_3O_4 and Fe_3O_4@Ag NPs are shown by SEM in Fig. 1A and B. The Fe_3O_4@Ag NP nanostructures are spherical and relatively uniform in size with an average diameter of approximately 350 nm, in which a number of small Ag NPs are located on the surface of the Fe_3O_4 NPs. The Ag satellite NPs around the Fe_3O_4 core have an average diameter of about 20 nm, as displayed in the TEM images in Fig. 1C and D. The elemental mapping analysis demonstrated that Fe, O and Ag were the major elements (Fig. 1E), and the elemental distribution of the Fe_3O_4@Ag core–satellite NPs is depicted in Fig. 1F–H. It can be clearly observed that the elements of Fe and O were homogenously

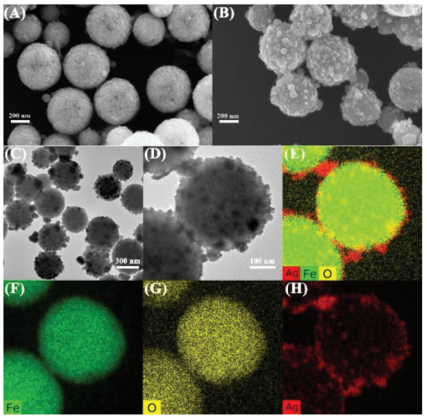

Fig. 1 SEM images of Fe_3O_4 NPs (A) and Fe_3O_4@Ag NPs (B). TEM images of the prepared Fe_3O_4@Ag core–satellite NPs at different magnifications (C and D). Mixed element mapping images of Fe, O and Ag (E), and element mapping images of Fe (F), O (G) and Ag (H) elements in the Fe_3O_4@Ag NPs corresponding to (D).

distributed throughout the Fe_3O_4 NPs, while the Ag satellite NPs were formed in the outer surface of the Fe_3O_4 core.

The XRD patterns of the prepared Fe_3O_4 and Fe_3O_4@Ag NPs further confirmed that the Ag satellite NPs were formed on the surface of the Fe_3O_4 NPs (Fig. S1A†). The characteristic diffraction peaks of the crystalline Fe_3O_4 NPs (curve a) at 30.3°, 35.4°, 43.2°, 56.9° and 62.5°, corresponding to the (220), (311), (400), (511) and (440) planes of the crystalline Fe_3O_4 NPs, can be obviously found.[34] After the Ag NPs were reduced onto the surface of the Fe_3O_4 NPs to form Fe_3O_4@Ag core–satellite NPs, several extra diffraction peaks at 38.2°, 44.3° and 64.5°, assigned to the (111), (200) and (220) planes of the Ag nanocrystals, appeared.[35] In addition, the magnetic hysteresis loops of the synthesized Fe_3O_4 and Fe_3O_4@Ag NPs that nearly intersect with the origin exhibit superparamagnetic behavior and little hysteresis, as shown in Fig. S1B.† The magnetic saturation (MS) value of the Fe_3O_4@Ag NPs was strong enough for magnetic separation from the solution during sample preparation processes.

3.2. Peroxidase catalytic activity of the Fe_3O_4@Ag NPs

The peroxidase-like activity of the Fe_3O_4@Ag NPs was investigated by the catalytic oxidation of the peroxidase substrate TMB in the presence of H_2O_2, as shown in Fig. 2. It is found that the Fe_3O_4@Ag NPs exhibited excellent catalytic capability with the existence of H_2O_2, which is nearly equal to that of a natural enzyme, HRP (Fig. 2A). The substrate TMB was oxidized acceleratively to produce an obvious blue color, with a maximum absorption peak at 652 nm (inset in Fig. 2).[36] In contrast, no obvious color change was observed in the blank system without TMB (curve c in Fig. 2A) and the reaction systems containing either Fe_3O_4@Ag NPs or H_2O_2 with TMB (curve a and b). Then, we investigated the catalytic reaction at different times by UV-vis spectroscopy to optimize the reaction time (Fig. 2B). As the reaction time was prolonged, the pro-

 This journal is © The Royal Society of Chemistry 2022

Published on 17 Februarie 2022. Downloaded on 2025-08-07 10:22:05 vm..

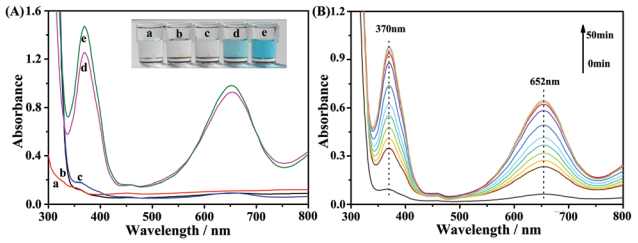

Fig. 2 (A) UV-vis absorption spectra of the reaction systems with different reagents: (a) TMB + Fe_3O_4@Ag, (b) TMB + H_2O_2, (c) H_2O_2 + Fe_3O_4@Ag, (d) TMB + H_2O_2 + Fe_3O_4@Ag and (e) TMB + H_2O_2 + HRP. The inset shows the corresponding color of the solutions. (B) The UV-vis absorption spectra of TMB catalyzed by Fe_3O_4@Ag NPs in the presence of H_2O_2 at different times in the range of 0–50 min with an increment of 5 min.

duced oxidized TMB (oxTMB) and the corresponding characteristic absorbance increased. After 40 min of reaction, the absorbance of oxTMB tended to be stable. We then chose 40 min as the optimal reaction time for the subsequent kinetic analysis of the Fe_3O_4@Ag NP-catalysed reaction.

3.3. Kinetic analysis and mechanism investigation of the Fe_3O_4@Ag NPs as peroxidase mimics

The Fe_3O_4@Ag NP-based catalytic reaction under different pH (2–9) conditions was investigated (Fig. S2A†). The Fe_3O_4@Ag NPs exhibited the maximum activity in a relatively wide pH range from 4 to 7, in view of the characteristic absorption at 625 nm. Then, the effect of the concentrations of H_2O_2 and TMB was studied (Fig. S2B and C†). An obvious increase in the catalytic activity of the Fe_3O_4@Ag NPs was observed as the concentration of TMB and H_2O_2 increased. When the concentrations of TMB and H_2O_2 reached 1.5 mM and 2.5 mM, respectively, the Fe_3O_4@Ag NPs achieved the maximum peroxidase-like activity. However, the catalytic activity of the Fe_3O_4@Ag NPs declined slightly at higher concentrations of TMB (>1.5 mM) and H_2O_2 (>2.5 mM) in the reaction system, due to the competition for single catalytic sites. Thus, the TMB concentration of 1.5 mM and the H_2O_2 concentration of 2.5 mM were taken as the optimum conditions for subsequent kinetic analysis.

The steady-state kinetics of TMB oxidation using Fe_3O_4@Ag NPs was investigated. First, the concentrations of H_2O_2, as the substrate, were changed from 0.1 to 1.2 mM L^{-1} with a constant concentration of TMB (1.5 mM) to investigate the peroxidase-like activity of the Fe_3O_4@Ag NPs. Then, like the procedure above-mentioned, the concentrations of TMB, as the substrate, were changed in a range from 0.1 to 1.2 mM L^{-1} with a fixed concentration of H_2O_2 (2.5 mM) to study the affinity of the Fe_3O_4@Ag NPs for TMB. The steady-state kinetic parameters for the reaction were determined using the Michaelis–Menten equation,[37] $V = V_{max}\cdot[S]/(K_m + [S])$, where V is the initial catalytic velocity, V_{max} is the maximal velocity of reaction, [S] is the substrate concentration, and K_m is the Michaelis–Menten constant.

A series of initial rates were calculated from the time-dependent absorbance at 652 nm based on the molar absorption coefficient for oxTMB ($\varepsilon_{650\,nm} = 3.9 \times 10^4\ M^{-1}\ cm^{-1}$).[38]

As shown in Fig. 3A and B, typical Michaelis–Menten curves were acquired for the Fe_3O_4@Ag NPs with either TMB or H_2O_2 as a peroxidase substrate. The Michaelis–Menten constants (K_m) and maximum velocity (V_{max}) can be calculated from the Lineweaver–Burk double reciprocal plots (Fig. 3C and D) and are summarized in Table S1.† The K_m value represents the affinity of the enzyme to the substrate. A low K_m value indicates a high affinity and *vice versa*. The V_{max} value reflects the enzymatic catalytic activity.[33,37] It can be observed from Table S1† that the K_m value of the Fe_3O_4@Ag NPs to TMB is slightly higher than that of HRP, indicating that the Fe_3O_4@Ag NPs have comparable affinity for TMB with that for HRP. However, the K_m value of the Fe_3O_4@Ag NPs to H_2O_2 is higher than that of HRP, suggesting that the catalytic activity of the Fe_3O_4@Ag NPs was more stable at high H_2O_2 concentrations than that of HRP. The results of the kinetic study demonstrated that the Fe_3O_4@Ag NPs possessed high peroxidase-like activity.

In general, the oxidation of TMB is closely related to the hydroxyl radical (˙OH) generated from the nanomaterial-based peroxidase mimics. To confirm the formation of ˙OH, a TA test by fluorescence spectroscopy was conducted, in which TA captured ˙OH and reacted with it to form a highly fluorescent product of 2-hydroxy terephthalic acid (HTA).[33] No fluorescence peak appeared when the TA molecules reacted only with H_2O_2 (Fig. S3A(a)†). However, a distinct fluorescence peak was observed at 400 nm with the reaction system in the presence of the Fe_3O_4@Ag NPs and H_2O_2 (Fig. S3A(b)†), due to the formation of ˙OH resulting from the catalytic decomposition of H_2O_2 by the Fe_3O_4@Ag NPs. Meanwhile, such a TA test was also carried out by Raman spectroscopy (Fig. S3B†). A new band appeared at 1244 cm^{-1}, which was attributed to the C=C stretching vibration coupled with C–O–H stretching

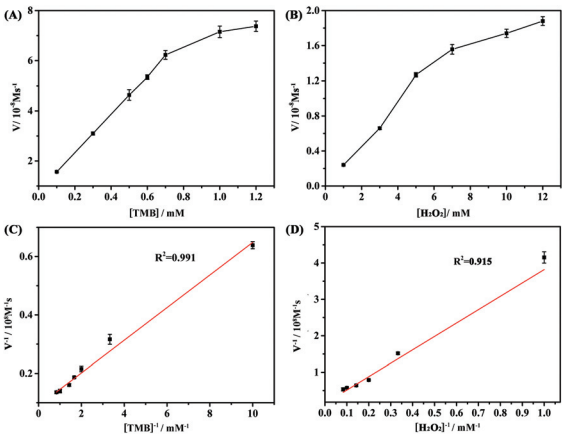

Fig. 3 Steady-state kinetic assay of Fe_3O_4@Ag core–satellite NPs for different components. (A and C) A fixed concentration of H_2O_2 (2.5 mM) with different concentrations of TMB. (B and D) A fixed concentration of TMB (1.5 mM) with different concentrations of H_2O_2.

Published on 17 Februarie 2022. Downloaded on 2025-08-07 10:22:05 vm..

vibration,[39,40] after introducing the Fe_3O_4@Ag NPs and H_2O_2 into the system. Such a change in the Raman spectra was further evidence for the generation of HTA from the TA.

The mechanism of the catalytic oxidation of TMB by the Fe_3O_4@Ag NPs in the presence of H_2O_2 can be ascribed to the two cascade steps as depicted in Scheme 1. First, the peroxidase-like activity of the Fe_3O_4 NPs allows the decomposition of the adsorbed H_2O_2 to generate $^{\bullet}OH$, followed by the Fenton-like reaction mechanism.[41] Moreover, the introduction of rich electronic Ag NPs is conducive to the electron transfer from Ag to Fe_3O_4,[42] which can accelerate the formation of $^{\bullet}OH$. Second, $^{\bullet}OH$ in the system can oxidize TMB to produce blue color oxTMB. Consequently, the Fe_3O_4@Ag NPs exhibit excellent peroxidase-like catalytic activity toward the oxidation of TMB by H_2O_2. Furthermore, the robustness and the stability of the Fe_3O_4@Ag NPs were studied by measuring the peroxidase-like activity of the Fe_3O_4@Ag NPs with long-term storage at room temperature, as shown in Fig. S4.† The peroxidase-like activity of the Fe_3O_4@Ag NPs remained almost intact over 4 weeks, which demonstrated that the Fe_3O_4@Ag NPs showed insensitivity to ambient conditions and exhibited remarkable stability.

3.4. SERS monitoring of the catalytic reaction of TMB by the Fe_3O_4@Ag NPs and SERS quantification of H_2O_2

In addition to the great peroxidase-like properties, the Fe_3O_4@Ag NPs have excellent SERS activity. Fig. 4A shows the changes in the SERS spectra during the catalytic oxidation of TMB in the presence of H_2O_2 catalyzed by the Fe_3O_4@Ag NPs at different times. Several new bands belonging to oxTMB at 1192, 1337, and 1611 cm^{-1} emerged with time, and were assigned to the CH_3 bending modes, inter-ring C–C stretching modes, and C–H bending coupled with ring stretching modes, respectively.[43] The intensities of such characteristic bands gradually increased with time, and tended to reach a maximum after reacting for 16 min (Fig. 4B), indicating that the catalytic reaction reached equilibrium in 16 min. Compared with the bulk phase catalytic reaction monitored by UV-vis methods (Fig. 4B), the reaction time was significantly reduced within the surface-catalyzed reaction monitored by SERS. The rapid response to H_2O_2 on the surface of the label-free Fe_3O_4@Ag NPs by SERS allows the H_2O_2 sensing, especially the intracellular H_2O_2 analysis.

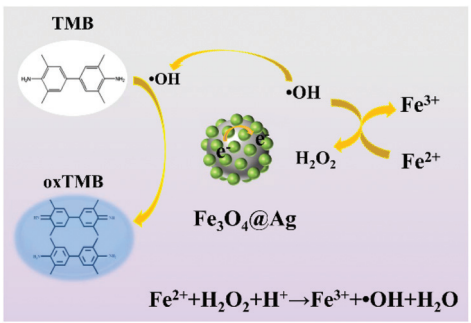

Scheme 1 An illustration of the catalytic oxidation of TMB by Fe_3O_4@Ag NPs.

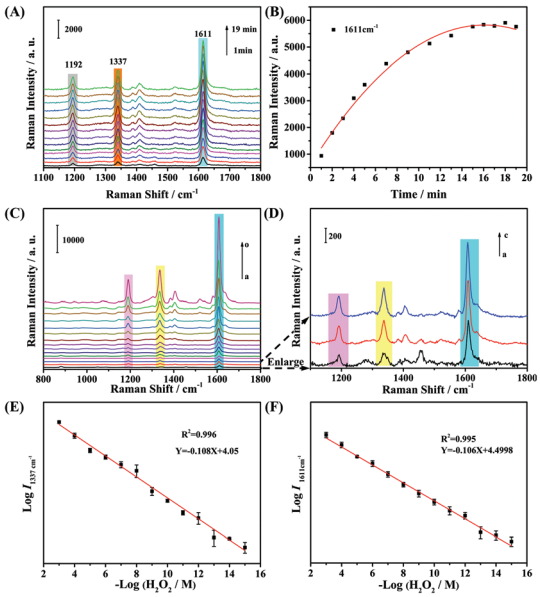

Fig. 4 (A) SERS monitoring of oxidized TMB molecules by H_2O_2 catalyzed by Fe_3O_4@Ag NPs. (B) The time-dependent variation of the SERS intensity of the band at 1611 cm^{-1}. (C) Concentration-dependent SERS spectra of TMB catalyzed by Fe_3O_4@Ag NPs in the presence of different concentrations of H_2O_2 (a: the blank sample; b–o: H_2O_2 concentration ranging from 10^{-15} to 10^{-3} M). (D) The enlarged spectra of a–c in the 1100–1800 cm^{-1} region in Fig. 4C. The plot of the logarithm of SERS intensities of the bands at 1337 cm^{-1} (E) and 1611 cm^{-1} (F) *versus* the logarithm of H_2O_2 concentrations.

The relationship between the SERS intensities of oxTMB and the concentration of H_2O_2 was studied. As displayed in Fig. 4C and D, the intensities of the characteristic bands at 1192, 1337, and 1611 cm^{-1} increased significantly as the H_2O_2 concentration increased in the range of 10^{-15}–10^{-3} M. Moreover, there was a distinct response to H_2O_2 even at the fM level by this Fe_3O_4@Ag NP-based approach (Fig. 4D), manifesting its prominent sensitivity for the H_2O_2 determination. Subsequently, the SERS intensities of the bands at 1337 and 1611 cm^{-1} were selected to plot the calibration curves for the quantitative analysis of H_2O_2 (Fig. 4E and F). Remarkably, it revealed excellent linear correlations (R^2 = 0.996 for the band at 1337 cm^{-1}; R^2 = 0.995 for the band at 1611 cm^{-1}) between either of the SERS intensities and the concentrations of H_2O_2 over a wide concentration range (10^{-15}–10^{-3} M). Therefore, the Fe_3O_4@Ag NPs exhibit excellent catalytic properties to catalyze the oxidation of TMB in the presence of an ultra-low amount of H_2O_2, and were able to quantitatively detect H_2O_2 with high sensitivity, which provided a premise for the determination of H_2O_2 released from living cells and the imaging of intracellular H_2O_2.

3.5. Detection of H_2O_2 released from living B16 cells and *in situ* imaging of intracellular H_2O_2 in single B16 cells by SERS

In order to further evaluate the selectivity of the Fe_3O_4@Ag NPs towards H_2O_2, the SERS behavior of TMB including the

This journal is © The Royal Society of Chemistry 2022

Published on 17 Februarie 2022. Downloaded on 2025-08-07 10:22:05 vm..

Fe_3O_4@Ag NPs and the other co-existing anions (CO_3^{2-}, NO_2^-, NO_3^-, and SO_4^{2-}), cations (Na^+, K^+, Ca^{2+}, Fe^{2+}, and Fe^{3+}), thiols (GSH, L-Cys) and other oxidative species ($^1O_2$, $ONOO^-$, and $ROO^\bullet$) was investigated. As displayed in Fig. 5A, a lower concentration of H_2O_2 (50 μM) induced a dramatic enhancement in the SERS signal owing to the production of oxTMB. However, other interfering species caused a negligible SERS response. These results demonstrate that the Fe_3O_4@Ag NP-based strategy is highly selective for H_2O_2 compared to other species, leading to highly sensitive H_2O_2 detection in the complex biological sample. The cellular toxicity of the Fe_3O_4@Ag NPs toward B16 cells was investigated using the MTT assay (Fig. S5†). The cellular viability decreased slightly after the cells were incubated with the Fe_3O_4@Ag NPs for 24 h with a concentration ranging from 1 to 5 μg mL^{-1}. Therefore, the Fe_3O_4@Ag NPs are of low toxicity with good biocompatibility, and thus can be used for intracellular H_2O_2 determination and cellular imaging analysis.

The applicability of the label-free bifunctional Fe_3O_4@Ag NPs to H_2O_2 in cells was explored by choosing B16 cells as the model cell line. PMA was used to stimulate living cells to produce H_2O_2 as the stimulant, while HRP was used as a scavenger of H_2O_2 to eliminate the H_2O_2 generated by the stimulation of PMA.[44] The SERS spectra of TMB within PBS (pH = 7.4) containing 5×10^6 B16 cells and the Fe_3O_4@Ag NPs without (the blank group) and with (the experiment group) the treatment of PMA were measured to investigate the H_2O_2 released from living B16 cells. Additionally, the SERS spectra of the B16 cells containing TMB and the Fe_3O_4@Ag NPs that were treated with HRP before the simulation of PMA were collected as a control group. Fig. 5B shows the typical SERS bands of oxTMB which increased significantly after treatment with PMA (curve b), demonstrating the generation of H_2O_2. In comparison, the SERS intensity of the blank group with the B16 cells incubated with TMB and the Fe_3O_4@Ag NPs (Fig. 5B(a)) was obviously lower than that of the experiment group under the same conditions. This indicated the insufficiency of the H_2O_2 generated from the B16 cells without the simulation of PMA to oxidize TMB under the catalysis of the Fe_3O_4@Ag NPs. Moreover, when HRP was added into the B16 cells in advance

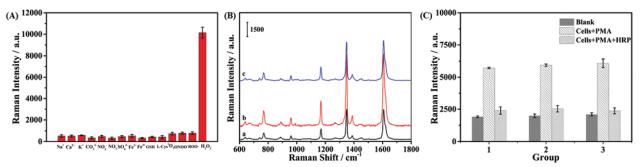

Fig. 5 (A) SERS response of TMB containing the Fe_3O_4@Ag NPs to the reaction of various interfering species: anions (1 mM for CO_3^{2-}, NO_2^-, NO_3^-, and SO_4^{2-}), cations (1 mM for Na^+, K^+, Ca^{2+}, Fe^{2+}, and Fe^{3+}), thiols (1 mM for GSH and L-Cys) and oxidative species (50 μM for $^1O_2$, $ONOO^-$, $ROO^\bullet$, and H_2O_2). (B) SERS spectra of TMB catalyzed by Fe_3O_4@Ag NPs with B16 cells (curve a), the cells after being treated with PMA (curve b), and the cells treated with HRP in advance of PMA stimulation (curve c), respectively. (C) The corresponding histogram of the change in the SERS intensity of the band at 1611 cm^{-1} in Fig. 5B from the three parallel groups of B16 cells.

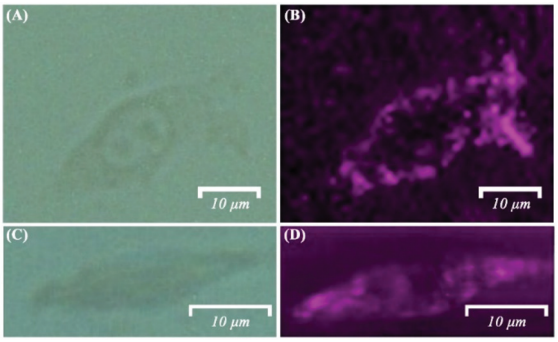

Fig. 6 Bright-field (A and C) and SERS mapping (B and D) images of two living B16 cells after treatment with PMA for 1 h at 37 °C. The SERS mapping images were generated with the intensity of the band at 1337 cm^{-1}.

of the PMA simulation, the SERS intensity of the control group (curve c) distinctly decreased to nearly the same value of that of the blank group, demonstrating that the increase of the SERS intensity in the experiment group (curve b) was caused by the H_2O_2 released from the B16 cells. The plotted standard curves in Fig. 4E and F were utilized to evaluate the H_2O_2 amount released from the single cell. It was calculated that the H_2O_2 released from each B16 cell was about 2.03×10^{-15} mol, which is consistent with the result reported in the earlier literature.[44] To verify the reproducibility of such a Fe_3O_4@Ag NP-based SERS method for the detection of H_2O_2 released from living cells, we collected the SERS spectra after the stimulation of PMA and HRP from three groups of the B16 cell samples, which were from different cell batches (Fig. 5C). The similar results from different B16 cell batches showed that the label-free Fe_3O_4@Ag NP-based SERS method for the intracellular H_2O_2 determination is reliable.

The label-free bifunctional Fe_3O_4@Ag NPs were then applied for the SERS imaging of single B16 cells to acquire the level of both intracellular and extracellular H_2O_2 concentrations. Fig. 6 displays the bright field and SERS mappings of the B16 cells after the stimulation of PMA. The cell profile in the SERS mapping images (Fig. 6B and D) is clearly observed and well-matched with the bright-field microscopy image (Fig. 6A and C) of the B16 cells. The SERS mapping images demonstrated that intracellular H_2O_2 was produced and accumulated under the stimulation of PMA. Moreover, extracellular H_2O_2 released from the B16 cells was also observed after the cells were treated with PMA, as shown in Fig. 6B and D. These results indicated that the visualization of the levels and the distributions of intracellular and extracellular H_2O_2 were possible to be achieved by such label-free bifunctional Fe_3O_4@Ag NP-based SERS methods.

4. Conclusions

In summary, label-free bifunctional Fe_3O_4@Ag NPs were successfully prepared for *in situ* imaging and determination of the

Published on 17 Februarie 2022. Downloaded on 2025-08-07 10:22:05 vm..

intracellular H_2O_2 level in single living cancer cells by SERS spectroscopy. The prepared Fe_3O_4@Ag NPs not only can offer a remarkable SERS enhancement but also exhibit excellent peroxidase-like catalytic activity toward the oxidation of TMB in the presence of H_2O_2. Additionally, they show long-term stability compared with the natural enzyme HRP and low cytotoxicity. The mechanistic studies of the catalytic activity demonstrated the capacity of Fe_3O_4@Ag NPs to decompose H_2O_2, in which $^{\bullet}OH$ was generated to oxidize TMB. The prepared Fe_3O_4@Ag NPs, without the modification of any label, were successfully applied to the specific detection of H_2O_2 in a wide linear range from 1 fM to 1 mM by SERS, and they even exhibited an excellent response to H_2O_2 at the fM level. Furthermore, *in situ* SERS imaging and quantification of intracellular H_2O_2 in single living B16 cells were achieved after stimulating the cells with PMA using the label-free Fe_3O_4@Ag NP-based SERS strategy. What's more, the visualization of the extracellular H_2O_2 that was released from the B16 cells was also achieved. This work provided promising *in situ* visualization of the intracellular H_2O_2 level in single cells, which is very critical for the early diagnosis and effective follow-up therapy of diseases involving changes in the physiological H_2O_2 level. Our proposed label-free nanosensor-based strategy can be extended to monitor and track cellular processes for fundamental research and clinical applications.

Author contributions

Yue Wang: conceptualization, methodology, funding acquisition, and writing – original draft. Cheng Cheng: methodology, formal analysis, writing – original draft, and visualization. Ruofei Ma: investigation and software. Zhangrun Xu: resources, funding acquisition, and supervision. Yukihiro Ozaki: supervision and writing – review and editing.

Conflicts of interest

There are no conflicts to declare.

Acknowledgements

This research was supported by the National Natural Science Foundation (Grant No. 21705015, 21874015, and 21675020) of P. R. China, the Fundamental Research Funds for the Central Universities (N2005020) and the Open Project of State Key Laboratory of Supramolecular Structure and Materials (Grant No. sklssm2021024).

Notes and references

1 M. Giorgio, M. Trinei, E. Migliaccio and P. G. Pelicci, *Nat. Rev. Mol. Cell Biol.*, 2007, **8**, 722–728.
2 K. Cui, C. Fan, G. Chen, Y. Qiu, M. Li, M. Lin, J. B. Wan, C. Cai and Z. Xiao, *Anal. Chem.*, 2018, **90**, 12137–12144.
3 E. Veal and A. Day, *Antioxid. Redox Signaling*, 2011, **15**, 147–151.
4 D. J. Zheng, Y. S. Yang and H. L. Zhu, *TrAC, Trends Anal. Chem.*, 2019, **118**, 625–651.
5 R. Shen, P. Liu, Y. Zhang, Z. Yu, X. Chen, L. Zhou, B. Nie, A. Żaczek, J. Chen and J. Liu, *Anal. Chem.*, 2018, **90**, 4478–4484.
6 W. Li, M. Khan, L. Lin, Q. Zhang, S. Feng, Z. Wu and J. M. Lin, *Angew. Chem., Int. Ed.*, 2020, **59**, 9282–9287.
7 H. Du, X. Zhang, Z. Liu and F. Qu, *Chem. Commun.*, 2019, **55**, 9653–9656.
8 E. K. Neumann, T. D. Do, T. J. Comi and J. V. Sweedler, *Angew. Chem., Int. Ed.*, 2019, **58**, 9348–9364.
9 C. Zhang, S. Yao, C. Xu, Y. Chang, Y. Zong, K. Zhang, X. Zhang, L. Zhang, C. Chen, Y. Zhao, H. Jiang, X. Gao and Y. Wang, *Anal. Chem.*, 2021, **93**, 1237–1241.
10 H. Gao, W. Han, H. Qi, Q. Gao and C. Zhang, *Anal. Chem.*, 2020, **92**, 8278–8284.
11 J. Xing, Q. Gong, O. U. Akakuru, C. Liu, R. Zou and A. Wu, *Nanoscale*, 2020, **12**, 24311–24330.
12 D. Kim, N. Oh, K. Kim, S. Lee, C. G. Pack, J. H. Park and Y. Park, *Methods*, 2018, **136**, 160–167.
13 H. R. Jia, Y. X. Zhu, Q. Y. Duan and F. G. Wu, *Chem. Soc. Rev.*, 2021, **50**, 6240–6277.
14 N. Ji, J. C. Magee and E. Betzig, *Nat. Methods*, 2008, **5**, 197–202.
15 L. Rodriguez-Lorenzo, K. Fytianos, F. Blank, C. von Garnier, B. Rothen-Rutishauser and A. Petri-Fink, *Small*, 2014, **10**, 1341–1350.
16 D. Cialla-May, X. S. Zheng, K. Weber and J. Popp, *Chem. Soc. Rev.*, 2017, **46**, 3945–3961.
17 M. Procházka, *Surface-Enhanced Raman Spectroscopy: Bioanalytical, Biomolecular and Medical Applications*, Springer International Publishing, Switzerland, 2016.
18 D. J. de Aberasturi, M. Henriksen-Lacey, L. Litti, J. Langer and L. M. Liz-Marzán, *Adv. Funct. Mater.*, 2020, **30**, 1909655.
19 D. J. De Aberasturi, A. B. Serrano-Montes, J. Langer, M. Henriksen-Lacey, W. J. Parak and L. M. Liz-Marzán, *Chem. Mater.*, 2016, **28**, 6779–6790.
20 K. Kneipp, Y. Ozaki and Z. Q. Tian, *Recent Developments in Plasmon-Supported Raman Spectroscopy*, World Scientific Publishing Europe Ltd, London, 2018.
21 Y. Wang, X. Zhao, Z. Yu, Z. Xu, B. Zhao and Y. Ozaki, *Angew. Chem., Int. Ed.*, 2020, **59**, 19079–19086.
22 K. A. Willets and R. P. Van Duyne, *Annu. Rev. Phys. Chem.*, 2007, **58**, 267–297.
23 Y. Liu, H. Ma, X. X. Han and B. Zhao, *Mater. Horiz.*, 2021, **8**, 370–382.
24 X. X. Han, W. Ji, B. Zhao and Y. Ozaki, *Nanoscale*, 2017, **9**, 4847–4861.
25 Y. Wang, J. Liu, X. Zhao, C. Yang, Y. Ozaki, Z. Xu, B. Zhao and Z. Yu, *Chem. Commun.*, 2019, **55**, 9697–9700.
26 X. Y. Zhao, G. Wang and M. Hong, *Mater. Chem. Phys.*, 2018, **214**, 377–382.

 This journal is © The Royal Society of Chemistry 2022

Published on 17 Februarie 2022. Downloaded on 2025-08-07 10:22:05 vm..

27 M. T. Alula and M. L. Madingwane, *Sens. Actuators, B*, 2020, **324**, 128726.
28 C. Wang, S. Xu, K. Zhang, M. Li, Q. Li, R. Xiao and S. Wang, *J. Mater. Sci.*, 2017, **52**, 1357–1368.
29 M. T. Alula and M. L. Madingwane, *Sens. Actuators, B*, 2020, **324**, 128726.
30 J. Liu, R. Che, H. Chen, F. Zhang, F. Xia, Q. Wu and M. Wang, *Small*, 2012, **8**, 1214–1221.
31 H. Cai, X. An, J. Cui, J. Li, S. Wen, K. Li, M. Shen, L. Zheng, G. Zhang and X. Shi, *ACS Appl. Mater. Interfaces*, 2013, **5**, 1722–1731.
32 N. R. Jana, L. Gearheart and C. J. Murphy, *Langmuir*, 2001, **17**, 6782–6786.
33 S. R. Ahmed, J. Cirone and A. Chen, *ACS Appl. Nano Mater.*, 2019, **2**, 2076–2085.
34 C. Hui, C. Shen, J. Tian, L. Bao, H. Ding, C. Li, Y. Tian, X. Shia and H. J. Gao, *Nanoscale*, 2011, **3**, 701–705.
35 P. Prieto, V. Nistor, K. Nouneh, M. Oyama, M. Abd-Lefdil and R. Díaz, *Appl. Surf. Sci.*, 2012, **258**, 8807–8813.
36 G. Fu, S. T. Sanjay, W. Zhou, R. A. Brekken, R. A. Kirken and X. Li, *Anal. Chem.*, 2018, **90**, 5930–5937.
37 O. Adeniyi, S. Sicwetsha and P. Mashazi, *ACS Appl. Mater. Interfaces*, 2020, **12**, 1973–1987.
38 R. J. Smith, P. J. King, M. Lotya, C. Wirtz, U. Khan, S. De, A. O'Neill, G. S. Duesberg, J. C. Grunlan, G. Moriarty, J. Chen, J. Wang, A. I. Minett, V. Nicolosi and J. N. Coleman, *Adv. Mater.*, 2011, **23**, 3944–3948.
39 F. Bardak, *J. Mol. Struct.*, 2019, **1175**, 458–470.
40 M. Karabacak, M. Cinar, Z. Unal and M. Kurt, *J. Mol. Struct.*, 2010, **982**, 22–27.
41 L. Gao, J. Zhuang, L. Nie, J. Zhang, Y. Zhang, N. Gu, T. Wang, J. Feng, D. Yang, S. Perrett and X. Yan, *Nat. Nanotechnol.*, 2007, **2**, 577–583.
42 H. Sun, X. Jiao, Y. Han, Z. Jiang and D. Chen, *Eur. J. Inorg. Chem.*, 2013, **1**, 109–114.
43 X. Ma, S. Wen, X. Xue, Y. Guo, J. Jin, W. Song and B. Zhao, *ACS Appl. Mater. Interfaces*, 2018, **10**, 25726–25736.
44 Y. Zhang, X. Bai, X. Wang, K. K. Shiu, Y. Zhu and H. Jiang, *Anal. Chem.*, 2014, **86**, 9459–9465.